Nanoscale

PAPER

View Article Online
View Journal | View Issue

Cite this: *Nanoscale*, 2019, **11**, 12230

Size-dependent exciton substructure in CdSe nanoplatelets and its relation to photoluminescence dynamics†

Judith F. Specht,[a] Riccardo Scott,[b] Marta Corona Castro,[a] Sotirios Christodoulou,[c,d] Guillaume H. V. Bertrand,[d,e] Anatol V. Prudnikau,[f] Artsiom Antanovich,[f] Laurens D. A. Siebbeles,[g] Nina Owschimikow,[b] Iwan Moreels,[d,h] Mikhail Artemyev,[f] Ulrike Woggon,[b] Alexander W. Achtstein *[b] and Marten Richter *[a]

CdSe nanoplatelets can be synthesized with different lateral sizes; very small nanoplatelets have almost quantum dot like features (almost discrete exciton states), while very large ones are expected to have properties of colloidal quantum wells (exciton continuum). However, nanoplatelets can be in an intermediate confinement regime with a rich substructure of excitons, which is neither quantum dot like nor an ideal 2D exciton. In this manuscript, we discuss the experimental transition energies and relaxation dynamics of exciton states in CdSe platelets with varying lateral dimensions and compare them with a microscopic theoretical model including exciton–phonon scattering. The model takes special care of the interplay of confinement and Coulomb coupling in the intermediate regime showing strong changes with respect to simple weak or strong confinement models by solving the full four dimensional lateral factorization free exciton wavefunction. Depending on the platelet size broad resonances previously attributed to just ground and excited states are actually composed of a rich substructure of several exciton states in their temporal dynamics. We show that these factorization free exciton states can explain the spectral features observed in photoluminescence experiments. Furthermore we demonstrate that the interplay of exciton bright and dark states provides principle insights into the overall temporal relaxation dynamics, and allows tuning of the exciton cooling *via* lateral platelet size. Our results and theoretical approach are directly relevant for understanding *e.g.* the size tuneability of lasing, excitonic cooling dynamics or light harvesting applications in these and similar 2D systems of finite lateral size.

Received 12th April 2019,
Accepted 11th June 2019

DOI: 10.1039/c9nr03161h

rsc.li/nanoscale

1. Introduction

Recently, semiconductor nanoparticles such as quasi-two-dimensional (2D) CdSe nanoplatelets (NPLs) have been synthesized and characterized[1–16] as well as hetero structures of them.[17–23] They constitute a novel class of colloidal 2D systems, developed after the synthesis of 0D and 1D systems,[24–27] whose unique optoelectronic properties can be controlled by composition, size, and shape and which may provide the colloidal counterpart to epitaxial quantum wells.[28–36] In contrast to transition metal dichalcogenides there is a defined control over the finite lateral size of the nanoplatelets. In particular, their lateral size can be tuned by the synthesis duration and proper choice of metal–organic precursors,[37] while the thickness is tunable to monolayer precision. Their lateral extent determines the physics between quantum well-like (weak confinement) and quantum dot-like (strong confinement) regimes.[38] As a consequence, the exciton

---

[a] *Institut für Theoretische Physik, Nichtlineare Optik und Quantenelektronik, Technische Universität Berlin, Hardenbergstr. 36, 10623 Berlin, Germany. E-mail: marten.richter@tu-berlin.de*
[b] *Institut für Optik und Atomare Physik, Technische Universität Berlin, Strasse des 17 Juni 135, 10623 Berlin, Germany. E-mail: achtstein@tu-berlin.de*
[c] *ICFO-Institut de Ciencies Fotoniques, 08860 Castelldefels, Barcelona, Spain*
[d] *Istituto Italiano di Tecnologia, IT-16163 Genova, Italy*
[e] *CEA Saclay, 91191 Gif-sur-Yvette, France*
[f] *Research Institute for Physical Chemical Problems of Belarusian State University, 220006 Minsk, Belarus*
[g] *Optoelectronic Materials Section, Delft University of Technology, 2629 HZ Delft, The Netherlands*
[h] *Department of Chemistry, Ghent University, Krijgslaan 281 - S3, 9000 Gent, Belgium*

† Electronic supplementary information (ESI) available: Additional details for the sample synthesis and characterization. See DOI: 10.1039/C9NR03161H

properties and dynamics in NPLs interpolate between the Coulomb- and confinement-dominated limits known from ideal quantum wells on the one hand and quantum dots on the other hand. This versatility makes them colloidally grown alternatives to epitaxial quantum wells or dots that are of interest, *e.g.*, for nanoscale light-emitters, efficient lasing or energy harvesting applications.

The optical response of these nano-emitters, *e.g.*, in photoluminescence (PL) experiments, is dominated by excitonic effects. The energetic separation between excitons,[38] the exciton–phonon interactions,[39] the dark–bright splitting of exciton states,[11] the oscillator strength and thus the radiative lifetime of excitons[39,40] strongly depends on the platelet lateral area. Therefore, varying the lateral size of these nano-objects provides a rich playground for optimizing the optoelectronic properties in terms of internal relaxation dynamics and exciton substructure.

In this article we compare a microscopic theoretical factorization free exciton substructure model to experimental time- and energy-resolved photoluminescence (PL) signals for different platelet sizes. Factorization free exciton eigenstates in this model are obtained from the full four-dimensional Schrödinger equations[38] and used to calculate the electron–phonon scattering rates. The full factorization free exciton eigenstates enable us to cover the full range of lateral sizes from weak (quantum well like) to strong confined (quantum dot like) structure, so that the usual approximate factorizations are not applicable. This yields a direct access to the exciton dynamics and the relaxation channels in the system, revealing the interplay of radiative and longitudinal-acoustic (LA) and -optical (LO) phonon scattering processes between the multiple center of mass bright and dark, discrete (small NPLs) and quasi-continuous (large NPLs) exciton states visible in the experimental data.

A direct comparison between theory and experiment at 4 K demonstrates that a large number of (center of mass) bright and dark exciton states contributes to the optical response revealing a substructure of exciton states inside the (double) emission peaks, without substructure so far attributed to ground and excited states for larger platelets.[39] In particular for small platelet sizes, phonon bottlenecks can trap the exciton population in higher exciton states, resulting in exciton lifetimes of the order of 100 ps, making these colloidal nanostructures interesting candidates *e.g.* for quantum-optical applications. The tunability of the cooling and decay dynamics *via* lateral size gives prospect to tunable excited state lasing or energy harvesting, and further involves the presence of center of mass momentum dark excitons altering the properties, as they provide non emitting exciton storage states, with a density of states controllable by the lateral size. In larger platelets the mentioned phonon bottlenecks are considerably weaker, so that the carrier cooling in the optically active states can be further tuned strongly by the lateral extent of the platelets allowing fast radiative recombination.

2. Experimental and theoretical model

CdSe nanoplatelets were synthesized and characterized by TEM, resulting in a series of nanoplatelets with 4.5 monolayer (ML) thickness and 17×6 nm^2 to 41×13 nm^2 lateral size. A dilute platelet solution without aggregates was dispersed in a polymer. The polymer was then deposited on fused silica substrates for low temperature PL measurements. This method avoids any potential stacking of nanoplatelets, thus a proposed excimer mechanism[41] for the phenomenological double emission of CdSe platelets does not apply for our experimental situation (see Methods section and ESI† for details).

2.1. Theoretical model system

Based on ref. 38, the nanoplatelets are modeled as quantum box like structures with a z confinement of few monolayers and a variable lateral (x, y) confinement chosen according to the experiment (size assessed from TEM measurements). We assume a two-band model in effective-mass approximation for the carriers and focus on exciton states around the band edge by restricting the calculation to the lowest electron and hole subbands. An orthonormal two-particle basis is introduced: $|\boldsymbol{k}_1, \boldsymbol{k}_2\rangle = a^\dagger_{\mathrm{c},\boldsymbol{k}_1} a_{\mathrm{v},\boldsymbol{k}_2}|0\rangle$, where $a^{(\dagger)}_{\lambda,\boldsymbol{k}}$ annihilates (creates) an electron with wave vector $\boldsymbol{k}$ in band λ = c, v and $|0\rangle$ denotes the electronic ground state.

Introducing an exciton basis $|\alpha\rangle$, the wave function $\Psi_\alpha(\boldsymbol{r}_\mathrm{e}, \boldsymbol{r}_\mathrm{h}) = \langle \boldsymbol{r}_\mathrm{e}, \boldsymbol{r}_\mathrm{h}|\alpha\rangle$ of exciton state α is factorized into an in-plane part $\psi_\alpha(\boldsymbol{\rho}_\mathrm{e}, \boldsymbol{\rho}_\mathrm{h})$ with $\rho_{\mathrm{e/h}} = \boldsymbol{r}_{\mathrm{e/h}_\parallel}$ and a perpendicular part $\zeta(z_{\mathrm{e/h}})$:[42] $\Psi_\alpha(\boldsymbol{r}_\mathrm{e}, \boldsymbol{r}_\mathrm{h}) = \psi_\alpha(\boldsymbol{\rho}_\mathrm{e}, \boldsymbol{\rho}_\mathrm{h})\zeta(z_\mathrm{e})\zeta(z_\mathrm{h})$. The z envelope is approximated by a Gaussian: $\zeta(z) = 1/(2\pi\sigma_z{}^2)^{1/4} e^{-z^2/4\sigma_z{}^2}$. The standard deviation $\sigma_z = z_0/3$ has been determined in a way that $\zeta^2(z_{\mathrm{e/h}})$ has almost decayed at the boarders of the platelet of width $z_0 = 0.302$ nm × 4.5 monolayers.[3] $\psi_\alpha(\boldsymbol{\rho}_\mathrm{e}, \boldsymbol{\rho}_\mathrm{h})$ solves the four-dimensional factorization free stationary Schrödinger equation for in-plane motion:[32,33,43]

$$\left(\frac{\hbar^2}{2m_\mathrm{e}}\nabla^2_{\rho_\mathrm{e}} - \frac{\hbar^2}{2m_\mathrm{h}}\nabla^2_{\rho_\mathrm{h}} + V_{\mathrm{c,e}}(\boldsymbol{\rho}_\mathrm{e}) + V_{\mathrm{c,h}}(\boldsymbol{\rho}_\mathrm{h}) + V_{\mathrm{e-h}}(\boldsymbol{\rho}_\mathrm{e} - \boldsymbol{\rho}_\mathrm{h})\right) \psi_\alpha(\boldsymbol{\rho}_\mathrm{e}, \boldsymbol{\rho}_\mathrm{h}) = E_\alpha \psi_\alpha(\boldsymbol{\rho}_\mathrm{e}, \boldsymbol{\rho}_\mathrm{h}). \tag{1}$$

Here, the first two terms describe the free motion of the electron and hole with effective mass $m_{\mathrm{e/h}}$ and E_α denotes the exciton binding energy. $V_{\mathrm{c,e}}(\boldsymbol{\rho}_\mathrm{e})$ and $V_{\mathrm{c,h}}(\boldsymbol{\rho}_\mathrm{h})$ are the lateral confinement potentials of the electron and hole, which are modeled as infinitely deep potential wells. $V_{\mathrm{e-h}}(\boldsymbol{\rho}_\mathrm{e} - \boldsymbol{\rho}_\mathrm{h})$ represents the attractive Coulomb interaction between the electron and the hole and is given as an effective in-plane potential[44]

$$V_{\mathrm{e-h}}(\boldsymbol{\rho}_\mathrm{e} - \boldsymbol{\rho}_\mathrm{h}) = -\frac{e^2}{4\pi\varepsilon_0\varepsilon} \frac{1}{\sqrt{(\boldsymbol{\rho}_\mathrm{e} - \boldsymbol{\rho}_\mathrm{h})^2 + (\alpha_0 z_0)^2}}, \tag{2}$$

where the parameter α_0 is adjusted to the width of the platelet in z direction using calculation for an ideal quantum well system as ref. 38. The eigenproblem of eqn (1) was solved numerically using finite differences for five different nanoplatelet sizes, ranging from 17 × 6 nm^2 to 41 × 13 nm^2 (analog to ref. 38). In eqn (1) the spin dependence was neglected implicitly restricting the dynamics to the bright spin-allowed states of platelets. This is justified, since we expect a relaxation to the spin-forbidden dark exciton states only on longer times[45] and here the focus is on shorter times scales (first hundred picoseconds). As a consequence for including only bright states exchange splitting effects are neglected, but we may comment on their different influence within our exciton substructure. Exchange effects play an important role for quantum dots and their level structure and dynamics. Since this paper aims for larger platelets (more quantum well like) and exchange effects are fast decreasing for increased system sizes, exchange effects are probably of minor importance for our qualitative results.[25,45,46] However the obtained exciton states show already distinct qualitative differences, so that a different behavior attributed to band mixing effects observed in a magnetic field[45] can be explained (see discussion section).

In this study, radiative and phonon-mediated exciton relaxation processes in CdSe nanoplatelets surrounded by oleic acid ligands are studied, therefore the Hamiltonian of the system transformed into the exciton basis introduced above includes:

$$\begin{aligned} H = {} & \sum_{\alpha} E_{\alpha} |\alpha\rangle\langle\alpha| + \sum_{\mathrm{j},\boldsymbol{q}} \hbar\omega_{\mathrm{j},\boldsymbol{q}} b^{\dagger}_{\mathrm{j},\boldsymbol{q}} b_{\mathrm{j},\boldsymbol{q}} + \sum_{\mathrm{l},\boldsymbol{q}} \hbar\omega_{q} c^{\dagger}_{\mathrm{l},\boldsymbol{q}} c_{\mathrm{l},\boldsymbol{q}} \\ & + \sum_{\alpha,\beta} \sum_{\mathrm{j},\boldsymbol{q}} g^{\alpha\beta}_{\mathrm{j},q} \left(b_{\mathrm{j},-\boldsymbol{q}} + b^{\dagger}_{\mathrm{j},\boldsymbol{q}} \right) |\alpha\rangle\langle\beta| \\ & + \sum_{\alpha} \sum_{\mathrm{l},\boldsymbol{q}} \left(M^{\alpha}_{\mathrm{l},\boldsymbol{q}} c^{\dagger}_{\mathrm{l},\boldsymbol{q}} |0\rangle\langle\alpha| + M^{\alpha *}_{\mathrm{l},\boldsymbol{q}} c_{\mathrm{l},\boldsymbol{q}} |\alpha\rangle\langle 0| \right). \end{aligned} \tag{3}$$

The Hamiltonian includes the electronic part with exciton energy E_{α}, the free phonon and photon contribution (second and third term), and the coupling to phonons and to the quantized light field (last two terms). $b^{(\dagger)}_{\mathrm{j},\boldsymbol{q}}$ denotes the bosonic annihilation (creation) operator for a phonon mode j with wave vector $\boldsymbol{q}$ and frequency $\omega_{\mathrm{j},\boldsymbol{q}}$. $c^{(\dagger)}_{\mathrm{l},\boldsymbol{q}}$ annihilates (creates) a photon of mode l, wave vector $\boldsymbol{q}$, and frequency $\omega_{\mathrm{q}} = cq/(\sqrt{\varepsilon_{\mathrm{r}}})$. The coupling elements formulated using the four dimensional exciton wave function are given in the ESI.†

The quantities of interest for the calculation of observables are the expectation values of the exciton density matrix elements. The exciton densities and polarizations are defined as $\rho_{\alpha\beta} = \mathrm{tr}_{\mathrm{B}}[\langle\beta|\rho|\alpha\rangle]$ and $\rho_{\alpha 0} = \mathrm{tr}_{\mathrm{B}}[\langle\phi_0|\rho|\alpha\rangle]$, where tr_{B} denotes the trace over the reservoir states. When deriving the equations of motion based on the von Neumann equation $i\hbar\partial_t\rho_{\mathrm{S}} = [H,\rho_{\mathrm{S}}]$ for the system density matrix, the hierarchy problem arising from the many particle coupling is solved by applying a Born–Markov treatment and assuming the phonons to be in thermal equilibrium at the experimental temperature of 4 K: $\langle b^{\dagger}_{\mathrm{j},\boldsymbol{q}} b_{\mathrm{j}',\boldsymbol{q}'}\rangle = \delta_{\boldsymbol{q},\boldsymbol{q}'}\delta_{\mathrm{j},\mathrm{j}'} n(\hbar\omega_{\mathrm{j},\boldsymbol{q}})$ with n denoting a Bose distribution. Therefore only single phonon scattering processes are included. This limits the validity of the model for acoustic phonon to low temperatures. Furthermore this leads for quantum dots (with large exciton energy spacing) to a phonon bottleneck, which is softened in the experiment by multiphonon effects, surface ligands *etc*. Especially surface ligands may be able to reduce or remove the phonon bottleneck, as discussed later for the quantum dot like platelet. Here we target larger platelets(more quantum well like with small exciton state energy spacing) for which the single phonon effects are the dominant process,[32,42] what can be also seen in the fact that the emission line width at low temperature is consistent with single acoustic phonon deformation potential scattering[47] and higher anharmonic terms are not needed to describe the linewidth. Overall this yields the following equations of motion for the exciton densities and polarizations:[32]

$$\frac{\partial}{\partial t}\rho_{\alpha\alpha} = -2R_{\alpha}\rho_{\alpha\alpha} + \sum_{\beta} \gamma_{\alpha\leftarrow\beta}\rho_{\beta\beta}, \tag{4}$$

$$\frac{\partial}{\partial t}\rho_{\alpha 0} = \left(\frac{i}{\hbar} E_{\alpha} - R_{\alpha} - \Gamma_{\mathrm{pd}} \right) \rho_{\alpha 0}. \tag{5}$$

Here Γ_{pd} is the phenomenological pure dephasing. The total out-scattering rate $R_{\alpha} = \frac{1}{2}\left(r_{\alpha} + \sum_{\beta} \gamma_{\beta\leftarrow\alpha} \right)$ is composed of the spontaneous radiative decay rate

$$r_{\alpha} = \frac{2\pi}{\hbar} \sum_{\mathrm{l},\boldsymbol{q}} |M^{\alpha}_{\mathrm{l},\boldsymbol{q}}|^2 \delta(E_{\alpha} - \hbar\omega_{q}) \tag{6}$$

and the phonon scattering rate

$$\begin{aligned} \gamma_{\beta\leftarrow\alpha} = \frac{2\pi}{\hbar} \sum_{\mathrm{j},\boldsymbol{q}} |g^{\beta\alpha}_{\mathrm{j},\boldsymbol{q}}|^2 \big\{ & (n_{\mathrm{j},\boldsymbol{q}} + 1)\delta(E_{\beta} - E_{\alpha} + \hbar\omega_{\mathrm{j},\boldsymbol{q}}) \\ & + n_{\mathrm{j},\boldsymbol{q}}\delta(E_{\beta} - E_{\alpha} - \hbar\omega_{\mathrm{j},\boldsymbol{q}}) \big\} \end{aligned} \tag{7}$$

consisting of Stokes (first term) and anti-Stokes contributions including acoustical and optical phonon scattering. The coupling elements are $g^{\beta\alpha}_{\mathrm{j},\boldsymbol{q}}$, see eqn (14)–(19). Note, that we include only first order, single phonon processes in our calculations. Inserting the expression for the optical matrix element in exciton basis (eqn (18)), converting the sum over $\boldsymbol{q}$ into an integral, and evaluating the δ function leads to the spontaneous decay rate[32]

$$r_{\alpha} = \frac{2d^2_{\mathrm{vc}}}{3\pi\varepsilon_0\varepsilon_{\mathrm{r}}\hbar} |\tilde{\psi}_{\alpha}(\boldsymbol{q}_{\parallel} = 0)|^2 K_0^3. \tag{8}$$

Here, $K_0 \equiv \frac{E_{\alpha}\sqrt{\varepsilon_{\mathrm{r}}}}{\hbar c}$ denotes the light cone and $\tilde{\psi}_{\alpha}(\boldsymbol{q}_{\parallel}) = \int d^2\rho\psi_{\alpha}(\boldsymbol{\rho},\boldsymbol{\rho})\mathrm{e}^{\mathrm{i}\boldsymbol{q}_{\parallel}\cdot\boldsymbol{\rho}}$ the Fourier transform of the exciton wave function for equally positioned electron and hole with zero center of mass momentum.

A similar procedure is applied to the phonon scattering rates in order to make them numerically tractable. The strict energy selection rule in the case of optical phonon scattering, the δ function, is replaced by a Gaussian function of width γ_{LO} = 0.5 meV to take dephasing due to acoustic phonons into account.[40] Fig. 1(a) shows the calculated phonon scattering rate $\gamma_{\beta\leftarrow\alpha}$ as a function of the energy difference E_{α}–E_{β} of the

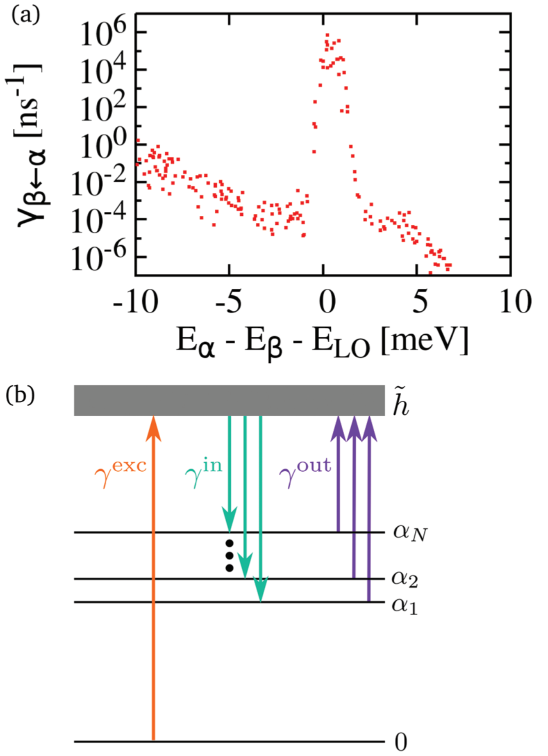

Fig. 1 (a) Calculated phonon scattering rate $\gamma_{\beta\leftarrow\alpha}$ of the 21 × 7 nm^2 platelet as a function of the energy difference $E_\alpha - E_\beta$ of the involved initial (α) and final states (β). The energy difference is plotted as detuning from the mean LO phonon energy $E_{LO} = \hbar(\omega_{LO}^\Gamma + \omega_{LO}^X)/2$. The increasing background is given by acoustic phonon scattering, which peaks zero absolute energy (−25.5 meV in this relative scale). (b) Schematic of the Lindblad processes involving the high-energy band $\tilde{h}$.

involved initial (α) and final exciton states (β). The phonon rate shows a clear resonance at the mean LO phonon energy E_{LO} = 25.5 meV, broadened by the softening parameter γ_{LO}. This indicates the existence of a phonon bottleneck since only few exciton states fulfill the required energy match. The asymmetric shape of the curve stems from the LA phonon coupling contribution that increases for decreasing energetic separations between the initial and final state, see eqn (15).

So far, the external photoexcitation of the platelets is not included in the equations of motion. In the considered spectroscopic experiment, the laser excitation takes place at energies far above the band gap. However, the available computational memory restricts the number of calculated exciton states to a limited number of states close to the band gap (40 states). In order to phenomenologically include the incoherent optical pumping, a Lindblad approach is chosen.[48,49] Therefore, the Lindblad dissipator $\mathscr{D}$ is introduced that modifies the von Neumann equation: $\frac{\partial}{\partial t}\rho_S = -\frac{i}{\hbar}[H,\rho_S] + \mathscr{D}\rho_S$ with

$$\mathscr{D}\hat{\rho}_S \equiv \sum_k \frac{\gamma_k}{2}\left(2A_k\rho_S A_k^\dagger - A_k^\dagger A_k\rho_S - \rho_S A_k^\dagger A_k\right). \qquad (9)$$

The Lindblad operators $A_k^{(\dagger)}$ describe processes that occur at a rate γ_k in the system. We have furthermore carefully checked, that enough exciton states are included, so that the results converged.

An ensemble of high-energy states in the nanoplatelet is introduced for a phenomenological treatment of the higher energy states above the calculated states. They are assumed to form a quasi-continuous band of high energetic states labeled $\tilde{h}$. At the initial time t_0 = 0, a Gaussian-shaped 150 fs laser pulse excites charge carriers from the ground state into the ensemble of high-energy band states modeled using a time-dependent rate γ^{exc}. The probability ensemble $\tilde{h}$ itself can interact with the exciton states α in two ways: first, the high-energy band states $\tilde{h}$ can decay into the states α under phonon emission at a rate γ_α^{in} and second, the states α can scatter into the high-energy band states $\tilde{h}$ by absorbing a phonon at rate γ_α^{out}. All rates are assumed to be mean values and therefore independent of the specific auxiliary state within the high-energy band $\tilde{h}$. The three processes, namely the optical pumping from the crystal ground state into the high-energy band and the in- and out-scattering between the high-energy states and the N numerically calculated lowest-energy excitons X_α are schematically depicted in Fig. 1(b).

The exciton populations $\rho_{\alpha\alpha}$ couple to the high-energy density $\rho_{\tilde{h}\tilde{h}}$, whose equation of motion is given by

$$\frac{\partial}{\partial t}\rho_{\tilde{h}\tilde{h}} = \gamma^{exc}\rho_{00} - \sum_\alpha \gamma_\alpha^{in}\rho_{\tilde{h}\tilde{h}} + \sum_\alpha \gamma_\alpha^{out}\rho_{\alpha\alpha}. \qquad (10)$$

ρ_{00} denotes the ground state population.

The in-scattering rate is assumed to follow a Gaussian distribution around the mean energy $E_{\tilde{h}}$ of the high-energy band: $\gamma_\alpha^{in} = \gamma_0^{LA}\exp[-(E_\alpha - E_{\tilde{h}})^2/\sigma_{\tilde{h}}^2]$. The mean energy $E_{\tilde{h}}$ and width $\sigma_{\tilde{h}}$ characterizing the high-energy band are modeled depending on the energy coverage $E_{\alpha N}$–$E_{\alpha 1}$ (with $E_{\alpha 1}$ and $E_{\alpha N}$ being the energies of the energetically lowest and highest calculated exciton states):

$$E_{\tilde{h}} = E_{\alpha N} + A(E_{\alpha N} - E_{\alpha 1}) \quad \text{with } A = 0.1, \qquad (11)$$

$$\sigma_{\tilde{h}} = BA(E_{\alpha N} - E_{\alpha 1}) \quad \text{with } B = 0.7. \qquad (12)$$

The parameters A and B are chosen in a way that the phenomenological high-energy band fully decays into the calculated exciton states within few ps (see below). We remark that the experimental observables are insensitive to these parameters. For the out-scattering rate, a detailed-balance expression is chosen: $\gamma_\alpha^{out} = \gamma_\alpha^{in}\exp[E_\alpha - E_{\tilde{h}}/(k_{BT})]$.

The resulting equation of motion are solved using a time-stepping Runge–Kutta solver from PETSc.[50,51] Finally, the time- and frequency-resolved detection signal for incoherent emission is calculated[32]

$$I_{l,\boldsymbol{q}}^{inc}(\omega,t) = \sum_\alpha \left|M_{l,\boldsymbol{q}}^\alpha\right|^2\left(\rho_{\alpha\alpha}(t) - |\rho_{\alpha 0}(t)|^2\right) \times \frac{R_\alpha + \Gamma_{pd}}{(\omega - E_\alpha/\hbar)^2 + (R_\alpha + \Gamma_{pd})^2} \qquad (13)$$

with the temperature-dependent pure dephasing rate $\Gamma_{pd}(T) = \Delta_0 k_B T/\hbar + \Gamma_{const}$. The linewidth of CdSe nanoplatelets at room temperature is less than ~40 meV,[2,52] so we can approximate the slope (related to the first term in the expression above) accordingly as $\Delta_0 \approx 1.5$. Furthermore, we set phenomenologically (the pure radiative contribution) $\Gamma_{\text{const}} = 2$ meV to be conservative to a low value, so that the exciton substructure is better resolved than in the experiment. This may underestimate the pure dephasing slightly, but is in good agreement with the ~3 meV reported for 5.5 ML platelets in ref. 52. The overall emission line width includes both pure dephasing and exciton–phonon scattering processes as well as radiative decay (see eqn (4)–(7)) and depends strongly on the actual emission state.

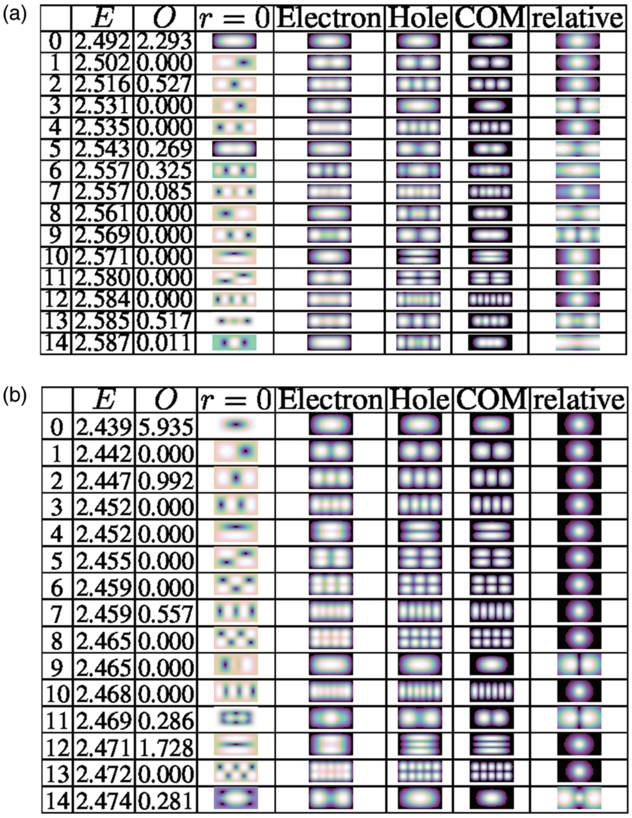

(a)

	E	O	$r = 0$	Electron	Hole	COM	relative
0	2.492	2.293					
1	2.502	0.000					
2	2.516	0.527					
3	2.531	0.000					
4	2.535	0.000					
5	2.543	0.269					
6	2.557	0.325					
7	2.557	0.085					
8	2.561	0.000					
9	2.569	0.000					
10	2.571	0.000					
11	2.580	0.000					
12	2.584	0.000					
13	2.585	0.517					
14	2.587	0.011					

(b)

	E	O	$r = 0$	Electron	Hole	COM	relative
0	2.439	5.935					
1	2.442	0.000					
2	2.447	0.992					
3	2.452	0.000					
4	2.452	0.000					
5	2.455	0.000					
6	2.459	0.000					
7	2.459	0.557					
8	2.465	0.000					
9	2.465	0.000					
10	2.468	0.000					
11	2.469	0.286					
12	2.471	1.728					
13	2.472	0.000					
14	2.474	0.281					

Fig. 2 Example exciton eigenstates of (a) 17 × 6 nm^2 and (b) 30 × 15 nm^2. Column *E* is the energy of the exciton. Column *O* is a measure for the oscillator strength in arbitary units. $r = 0$ is a plot of the diagonal wavefunction $\Psi(r, r)$ (electron and hole at the same position *r*), which gives integrated a measure of the oscillator strength.[38] Electron and hole column are the full exciton wavefunction traced out to electron and hole single particle function (useful in strong confinement) and COM and relative are the center of mass and relative mass wavefunction traced out from the full solution (usefull in weak confinement), *cf.* ref. 38.

3. Results & discussion

3.1. Time- and energy-resolved photoluminescence

In the following we analyze the experimental data and compare them to the results of our theoretical model to explain the underlying physics. In order to achieve this, the experimental data (right column) and the calculated time- and frequency-resolved PL signal of eqn (13) at 4 K are plotted in Fig. 3 (left column) for five different platelet sizes. An additional minor energy correction was used for each calculated PL signal adjusting the lowest theoretical energy to the experimental data including the *z* direction confinement. The linewidth of the experimental spectra is larger compared to simulation due to the additional inhomogeneous broadening present in the experiment and finite spectral resolution of the streak camera. Also the deliberately chosen smaller phenomenological pure dephasing in theory (used for plotting only to obtain a better resolution of the underlying exciton structure in Fig. 2) results in slightly smaller simulated line width.

The narrow PL lines of the calculated spectra allow to inspect a very important finding: in the experiment, a maximum of two separable exciton signatures is visible in the spectra, which has lead in ref. 39 to a first interpretation, that two exciton states of different energy, *e.g.* an exciton ground state (GS) and excited state (ES), are visible in PL. As we will see the full four-dimensional exciton calculation will change the picture slightly depending on the platelet size. With increasing platelet size, the GS and ES named signatures are hardly separable any more, but merge into one feature with a fast decaying high-energy shoulder within the first few ps after pulsed excitation (*cf.* Fig. 3(c–e), right column). However, a comparison to the calculated spectra (left column) reveals immediately that these one or two broadened main lines accessible in the experiment are actually composed of a bunch of different lines resulting from different bright exciton states (*cf.* the oscillator strength of the different states in Fig. 2) that are gradually populated after the arrival of the incoherent pump pulse. Furthermore the wavefunction diagonal in electron and hole $\Psi(\boldsymbol{r}, \boldsymbol{r})$ for the different (dark and bright) substructure exciton states does not only enter the oscillator strength *via* $\int \mathrm{d}\boldsymbol{r}\Psi(\boldsymbol{r},\boldsymbol{r})$, but also the exchange splitting *via* $\int \mathrm{d}\boldsymbol{r}|\Psi(\boldsymbol{r},\boldsymbol{r})|^2$ (*cf.* ref. 25 and 46) and thus may provide an alternative explanation to the magnetic field dependent experimental data in ref. 45 and its trion hypothesis, since the exciton states Fig. 2 in show different symmetries in $\Psi(\boldsymbol{r}, \boldsymbol{r})$. The energy spacing of the exciton states calculated (*cf.* Fig. 2) is consistent with other methods using Ansatz wave function with variational principles.[23] First, the optical pumping fills the energetically higher exciton states, which are phenomenologically included. With increasing time, they decay into the lower exciton states *via* phonon-scattering processes until the population resides mainly in the exciton ground state after roughly 100 ps. In the experimental data the behavior is visible in a change of the (shape of the) PL emission bands. This distinct exciton GS line is clearly visible also in the calculated spectra, but only for the smallest platelet only one exciton state contributes to the GS line as expected close to the strong confinement regime. Note, that for the 30 × 15 nm^2 platelet higher emitting states exist, but it can be seen that they contribute only very weakly due to fast relaxation into the GS in Fig. 3, both in simulation and experiment.

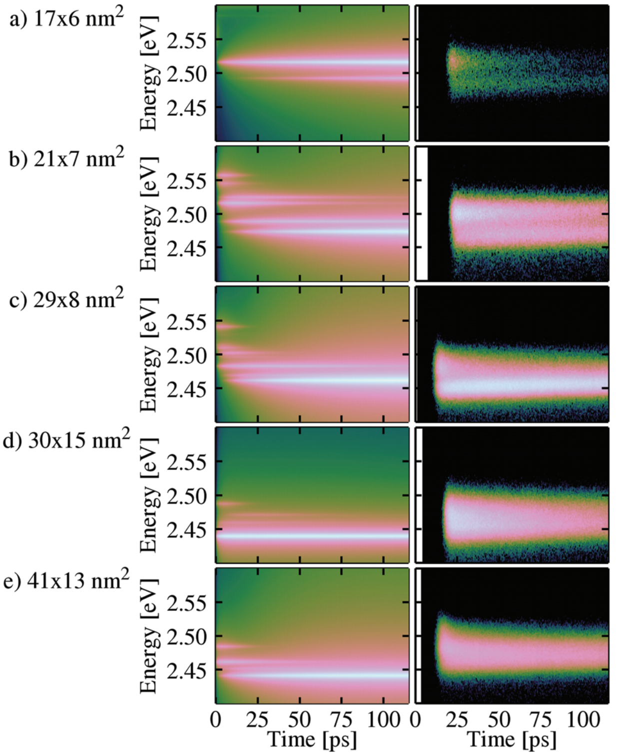

Fig. 3 Simulated PL time- and energy-resolved PL signals (left column) as well as experimental results (right column) for the different platelet sizes at 4 K, plotted on logarithmic scale. The time zero varies slightly in the right column due to slight variation of the relative phase of exciting pulsed laser and streak camera upon initial phase locking.

The theoretical model is build with the assumption of small exciton energy spacing, since larger platelets are in the focus of this paper, which are more quantum well like than quantum dot like. Therefore it comes with no surprise, that the largest qualitative difference between the experimental and theoretical data is found for the smallest 17 × 6 nm^2 platelet (Fig. 3(a)) which is more quantum dot like, where the calculation yields still a substantial population of the higher energy state that remains as long as 2 ns (not shown here), as opposed to a faster decay in the experimental data. So as already expected at the construction of the theoretical model, the typical phonon bottleneck effect is present, since we include only one phonon processes and the efficient transfer process present in the experiment is probably a multi-phonon process, that bridges the high energy spacings in the small platelet (some spacing are in the order of 10 meV). Furthermore in the experiment anharmonicity effects at the surfaces *e.g.* through ligands might open this decay channel and therefore may explain the qualitative differences in the long time behavior in addition to multiphonon processes. Therefore this behavior is not reflected in the experiment, where indeed in the beginning the intensity of the ES signal is larger compared to the GS, but the overall decay of both lines takes place on a much shorter timescale. However, the behavior is similar to mechanism observed experimentally in ref. 53.

Another aspect leading to the slow decay from the higher exciton state can be found in the symmetry of the wave function (*cf.* Fig. 2(a)). The state shows a p like symmetry so that the relative wavefunction is different to the other states, which may be another reason for temporal storage of the excitation in the simulation. In the experiment deviations from the ideal shape can lift the selection rules, which may open more relaxation channels.

However, also in the experiment, the signal intensity of the higher-energy ES feature relative to the GS line is decreasing with increasing platelet size: for smallest NPLs (Fig. 3(a) and (b)), the ES intensity dominates over the GS intensity, whereas for the intermediate platelet size 29 × 8 nm^2 (Fig. 3(c)), the initially weak ES exhibits a fast decay into the GS line that gains intensity very quickly (within few ps). Finally, for the large 30 × 15 nm^2 and 41 × 13 nm^2 NPLs (Fig. 3(d) and (e)), the intensity of the GS line is very strong right after pulse excitation, whereas the ES lines only appear as very short-lived high-energy shoulder. All trends visible in the measured PL spectra are clearly resembled in the simulations.

3.2. Temporal evolution of exciton populations

In order to analyze the processes inside the platelet a bit deeper, we have a look at the exciton dynamics used for the calculation of the exciton spectra. Therefore, we inspect snapshots of the populations of the calculated 40 lowest NPL exciton states as plotted over energy. For comparison, Fig. 4 shows the snapshots for the smallest, quantum-dot-like 17 × 6 nm^2 platelet and Fig. 6 displays the large 30 × 15 nm^2 platelet. We start with the discussion of the smallest platelet, Fig. 4. Eight snapshots are shown, beginning at 2 ps after the initial pulse excitation and ending at 1000 ps. The orange bars represent the oscillator strength of the respective exciton states and the blue bars depict the population. Within the first 20 ps (upper four snapshots), the highest calculated exciton state at 2.656 eV exhibits a significant occupation that is refilled from the initially excited high-energy reservoir (see the center energy of the reservoir in eqn (11)). During the same time, a gradual build-up of some of the lower-energy exciton populations can be observed. In particular the fourth exciton state at 2.662 eV develops a high population. This is particularly interesting since this is a dark exciton state with vanishing oscillator strength (*cf.* Fig. 2). This means that the phonon scattering into dark states plays a key role in the population distribution within the platelet. As a consequence, population trapping can occur since the dark states cannot decay radiatively. This effect is especially pronounced for the smaller platelets, since the reduced density of exciton states at lower energies removes decay channels due to acoustical phonons (open for larger platelets). Further relaxation due to optical phonons is not possible because of the high energy of optical phonons, which is larger than the exciton state spacing. Also, especially for the smallest, quantum dot like, platelets, where the energetic separation between the low exciton states is rather large due to the strong confinement, phonon scattering becomes inefficient: for example, the energetic distance between the above-

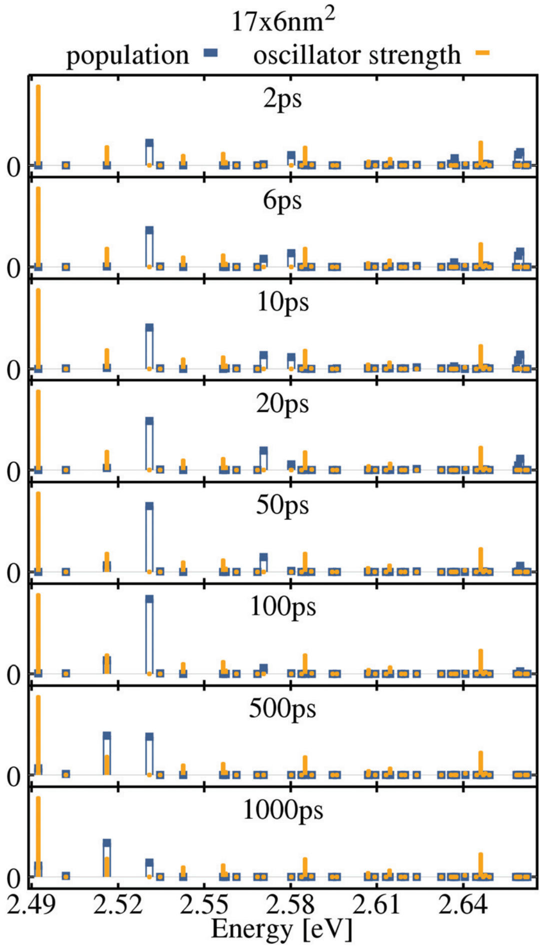

Fig. 4 Population snapshots for the 17 × 6 nm^2 platelet at 4 K. The constant oscillator strength (orange bars) and time-dependent population (blue bars) of the exciton states are depicted in arbitrary units in dependence of the energy.

mentioned highly populated fourth exciton state and the next lower third exciton state of the 17 × 6 nm^2 platelet is 15 meV (*cf.* Fig. 2). This is not enough to be bridged by LO phonons, however it is too large for LA phonons in single phonon approximation. Therefore, the population of this state can only be reduced by scattering first into higher-energy states and then decay from there towards the ground state, which is very unlikely at the considered low temperature of 4 K. Furthermore it may be reduced by the more p-like symmetry of the state in comparison to other states in this energy range (*cf.* Fig. 2).

This behavior of our theoretical model is expected, since we neglected multi-phonon processes in the model, which may be important for the quantum dot like platelet, since with a combination of multiple phonons the phonon bottleneck can be overcome. Therefore, the phonon bottleneck is less pronounced in the measured spectra since more decay channels are possible. This explains minor deviations between the exciton lifetimes observed in the experimental and calculated PL spectra.

The lower panels of Fig. 4 show that after 50 ps, the high exciton states have almost completely decayed and the population has been transferred to the low-energy excitons. However, for the above-mentioned reasons, even after 1 ns still some bright and dark exciton states are substantially populated. This changes in the case of the large 30 × 15 nm^2 platelet shown in Fig. 6: here, the exciton population has completely decayed after 500 ps. Due to the reduced lateral confinement, the exciton states are energetically much closer: whereas for the small 17 × 6 nm^2 platelet, the 40 lowest exciton states cover an energy range of 170 meV, this reduces to only 50 meV for the 30 × 15 nm^2 platelet. Hence, in the latter phonon scattering is more efficient since more phonon decay channels are allowed. Also for this NPL size, parts of the population are temporarily trapped in dark exciton states at energies of 2.452 meV and 2.455 meV. But the trapping does not prevail as long as in the smaller platelet due to missing phonon bottleneck, but may also be reduced due to similar symmetries visible in the traced out relative wave function (*cf.* Fig. 2).

Basically the small 17 × 6 nm^2 platelet is more quantum dot like, where the disappearance of the phonon bottleneck effect is often assigned to Auger[54–56] and also multiphonon effects. At low temperatures the acoustic phonon bottleneck

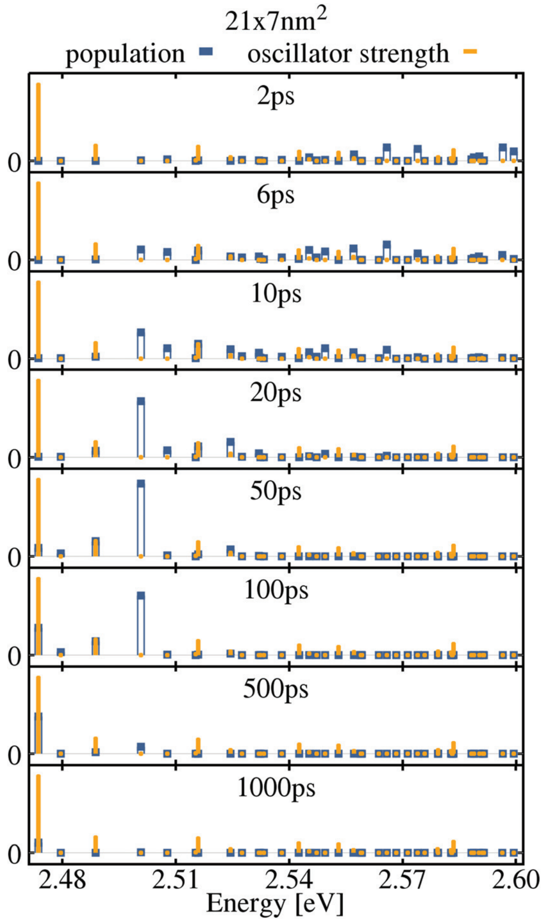

Fig. 5 Population snapshots for the 21 × 7 nm^2 platelet at 4 K. The constant oscillator strength (orange bars) and time-dependent population (blue bars) of the exciton states are depicted in arbitrary units in dependence of the energy.

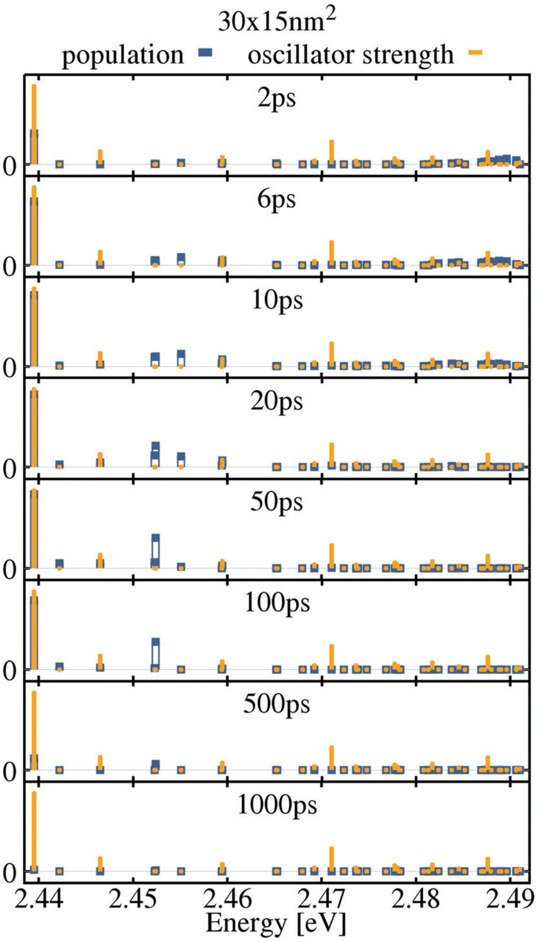

Fig. 6 Population snapshots for the 30 × 15 nm^2 platelet at 4 K. The constant oscillator strength (orange bars) and time-dependent population (blue bars) of the exciton states are depicted in arbitrary units in dependence of the energy.

effect was observed for example in ref. 57. However most platelets have more quantum wells like properties with higher exciton state density and the exciton–phonon processes included here are sufficient. For the quantum dot like platelet we remark that most of studies of QDs are at room temperature and thus the temporal dynamic is different to the experiments at low temperatures, presented here.

On the other hand the 21 × 7 nm^2 platelet as all of the other larger platelets does not show a phonon-bottleneck effect. However as one can see in Fig. 5 a substantial part of the population is stored in a dark state for hundreds of picoseconds and is feeding a bright excited state with lower energy as the dark state. This results in a higher PL emission at excited exciton states (*cf.* Fig. 3), whereas for the larger platelets the relaxation towards to the lowest exciton states is so efficient due to the increased density of states (*e.g.* 21 × 7 nm^2, 29 × 8 nm^2 platelets), that there the PL is dominated by the low energy excitons. We believe that the changes in the distribution of exciton populations due to exciton phonon scattering is also the reason for the predominant emission from the excited state at higher temperatures in experiments.[39,58] For example scattering to dark states, which may feed the excited state may be more efficient due to increasing density of states at elevated energies and an increased mean exciton energy in the distribution at elevated temperatures. However we can not explore this, since higher temperatures require multiphonon processes for acoustic phonons, which are not included in our model.

The tunability of recombination dynamics by lateral size, which we demonstrated in this paper can be important for the use of nanoplatelets *e.g.* in lasing applications, at least for low temperatures, where the excited state lifetime determines the inversion and gain that can be reached in the system. Further a rich sub structure not only of the mentioned exciton states obtained from a factorization free calculation, but also of biexcitons[59] and trions is expected in the nanoplatelets and similar 2D systems of finite lateral size.

We demonstrated that the exciton substructure resulting from the factorization free exciton calculation alone could explain the phenomenologically observed double emission of CdSe nanoplatelets and its' decay dynamics, however we do not exclude a potential additional emission contribution by charged exciton states (trions),[45,60] *e.g.* for small, more quantum dot like platelets, but we see qualitative differences in different exciton states, that may lead to different behavior in magnetic fields and not contradicting to the experimental data in ref. 45, however a detailed analysis is beyond the scope of the manuscript, since it is beyond available numerical resources. We would like to emphasis that unlike in ref. 60, where the platelets have been dropcasted directly on fused silica substrates, our nanoplatelets are embedded isolated in polymer. Dropcasting only may have an impact on potential charging of the nanoplatelets by ambient residual charges but also on potential stacking, which both are excluded in our samples using embedding isolated particles in polymer. Hence *e.g.* trions could contribute in different amount depending on sample preparation. However Diroll *et al.*[41] argue against trion formation that trion formation should be an instantaneous process for nanoplatelets containing an extra charge and that the trion lifetime should be shorter as the exciton lifetime in contrast to the slower rate constant found for the lower state in ref. 39. This is however not necessarily correct, as both exciton and trion state recombination undergo the Giant Oscillator Strength effect,[61] which has a different lateral platelet size dependence for both, potentially resulting in regions where the one or the other is the faster process.

Another hypothesis for the phonon replica based genesis[58] of the of the phenomenological double emission has already been shown to be unlikely in ref. 39, as the energy spacing varies from 18 to 38 meV by a factor of two with increasing lateral platelet size, much more than a phonon dispersion could allow. In published Raman data,[62] a LO-phonon energy of ∼25 meV has been measured for different nanoplatelets, in line with Table 1. Sigle *et al.*[63] have measured the that both confined in- and out of plane LO-phonon modes resemble the bulk dispersion quite well, so given the small energy scale of

Table 1 CdSe material parameters used for the calculation

Band gap[72]	E_g	1.84 eV
Mass density	ρ	5.82 g cm^{-3}
Interband dipole moment	d_{vc}	0.4 e nm
Heavy hole valence band eff. mass[73]	m_h	0.41 m_0
Conduction band eff. mass[73]	m_e	0.22 m_0
Sound velocity[74]	u	3.63 km s^{-1}
Static dielectric constant[39]	$\varepsilon_{\text{stat}}$	9.4
High-frequency dielectric constant[39]	ε_∞	7.9
Valence band deformation potential[18,75]	D_v	−3 eV
Conduction band deformation potential[18,75]	D_c	−6 eV
LO phonon frequency at Γ point[76]	$\omega_{\text{LO}}{}^{\Gamma}$	0.038 fs^{-1}
LO phonon frequency at X point[76]	$\omega_{\text{LO}}{}^{X}$	0.0396 fs^{-1}

the dispersion it can be excluded that an LO-phonon replica can cover up to 38 meV energy separation. This is in line with Diroll *et al.*,[41] who showed that the phenomenological energy spacing does not correlate with the Raman determined LO-phonon energy for platelet thickness variation. A potential excimer (charge transfer exciton) hypothesis,[41] where two attached platelets allow a charge transfer exciton state seems not applicable to our samples, as first by sample preparation stacking is excluded and secondly in contrast to Tessier *et al.*[58] we do not observe the there discussed characteristic constant energy spacing for varying lateral platelet dimensions. Furthermore since in the preparation stacking is more likely for large platelets, the effect should be strongly size dependent. Another point relates to the strongly extended nature of charge transfer (CT) excitons, the e–h envelope function overlap integrals should be considerably lower for CT exciton, and with them the radiative rates. Due to the reduced wavefunction overlap in a charge transfer state spanning to platelets a much slower exciton relaxation is expected. However that is not observed.[47]

4. Conclusions

In this manuscript, experimental time and energy resolved photoluminescence spectra were analyzed using a microscopic model for the exciton dynamics in CdSe nanoplatelets including radiative and phonon-assisted scattering processes for center of mass bright and dark states. The PL signals for five different platelet sizes were compared, showing a strong lateral size dependence of the phonon-scattering efficiency and the energy distribution of the exciton states resulting in a LO phonon bottleneck. Therefore, varying the lateral size of these nano-objects provides a rich playground for optimizing the optoelectronic properties in terms of internal relaxation dynamics of the factorization free exciton sub structure.

Based on our presented modeling, experimental results and the discussions of alternative explanations of the phenomenological double emission of CdSe nanoplatelets above, we advocate an exciton substructure as reason for the apparent double emission, explaining both energetic position and PL dynamics. Our findings suggest that the experimentally observed, strongly inhomogeneously broadened PL resonances are actually composed of several exciton resonances revealing an exciton substructure, that show strong qualitative difference, which should also result in different magnetic field properties. We argue that trion emission may occur additionally depending on sample preparation and experimental conditions, while excimer formation is unlikely in our isolated nanoplatelets in polymer, but may occur *e.g.* in concentrated colloidal dispersions.

Although only bright exciton states of the factorization free substructure are visible in the PL signal, the analysis of the temporal evolution of the exciton populations in our samples shows that also the exciton dark states have a major influence on the population dynamics. Population trapping occurs mainly in the small-sized platelets where phonon bottlenecks prevent the occupied dark states from decaying into lower exciton states. This effect is of course overestimated in the simulations since multi-phonon processes are not included in our model. However, all main trends observed in the experiment are reproduced and explained by the theoretical model, which uses the full factorization free four dimensional wavefunction covering weak-, intermediate and strong confinement regimes. The tunability of the dark and bright state dynamics allows to engineer *e.g.* excited or ground state lasing or the usage of nanoplatelets for solar energy harvesting applications. Further our theoretical model is fully transferrable to other 2D nanostructures, where finite lateral size effects gain increasing attention, like in transition metal dichalcogenides, allowing potentially to tune radiative rates and exciton phonon interaction.

5. Methods

5.1. Samples and setup

CdSe core NPls with the first exciton absorption bands around 512 nm (4.5 ML) were synthesized as described in ref. 6 and 12. Absorption and PL spectra as well as TEM images and details of the preparation avoiding any stacking effects can be found in the ESI.†

Our experimental setup allows for the measurement of time-integrated and -resolved fluorescence of a sample with confocal excitation (titanium sapphire laser (Coherent Mira 900F, FWHM 150 fs, 75.4 MHz) SHG at 420 nm) and detection through an objective (N.A. = 0.4). A spectrometer with an attached CCD (Roper Spec10) for time-integrated or a streak camera (Hamamatsu C5680) for time-resolved measurements is used. We applied a moderate CW equivalent 0.2 W cm^{-2} excitation density leading to <0.1 percent of the platelets to be excited within one laser pulse (average number of excitons per platelet per pulse below 10^{-3}). Details are given in the ESI.†

5.2. Coupling elements of the Hamilton operator

The phonon-coupling matrix element $g^{\alpha\beta}_{j,\boldsymbol{q}}$ in the exciton basis reads:[32]

$$g^{\alpha\beta}_{j,\boldsymbol{q}} = \hat{K}(q_z)\left(g_{c,j,\boldsymbol{q}}\hat{\chi}^{e}_{\alpha\beta}\left(\boldsymbol{q}_\parallel\right) - g_{v,j,\boldsymbol{q}}\hat{\chi}^{h}_{\alpha\beta}\left(\boldsymbol{q}_\parallel\right)\right) \tag{14}$$

with $\hat{K}(q_z) = \int \mathrm{d}z_\mathrm{e} \int \mathrm{d}z_\mathrm{h} \zeta^2(z_\mathrm{e})\zeta^2(z_\mathrm{h})\mathrm{e}^{\mathrm{i}q_z z_{\mathrm{e/h}}}$. The Fourier transformed projection of the in-plane wavefunction overlap integral on the electron/hole coordinate is defined as: $\hat{\chi}^{\mathrm{e/h}}_{\alpha\beta} = \int \mathrm{d}^2\rho_\mathrm{e} \int \mathrm{d}^2\rho_\mathrm{h} \psi^\star_\alpha(\boldsymbol{\rho}_\mathrm{e},\boldsymbol{\rho}_\mathrm{h})\psi_\beta(\boldsymbol{\rho}_\mathrm{e},\boldsymbol{\rho}_\mathrm{h})\mathrm{e}^{i\boldsymbol{q}\cdot\boldsymbol{\rho}_{\mathrm{e/h}}}$. It is calculated numerically. The matrix element for the deformation-potential coupling to longitudinal-acoustic (LA) phonons reads[64,65]

$$g^{\mathrm{LA}}_{\lambda,j,\boldsymbol{q}} = \sqrt{\frac{\hbar\omega_{j,\boldsymbol{q}}}{2\rho V u_\mathrm{j}^2}} D_\lambda \tag{15}$$

with quantization volume V, mass density ρ, sound velocity $u_\mathrm{j} = \omega_{\mathrm{j},q}/q$, and deformation potential D_λ. Note, that we assume bulk phonons, so that the quantization volume does not depend on the platelet size. The usage of bulk acoustic phonons for the acoustic coupling is further substantiated by recent emission line width investigations on CdSe nanoplatelets,[47] where an acoustic deformation potential of 3.0 ± 0.3 eV was found, in line with our assumptions in Table 1. Potential minor deviations may arise from contributions of ligand and host polymer vibrational modes but we do not expect qualitative differences as the acoustic coupling has been shown to be deformation potential like. We remark that bulk phonons are often also used as first approximation in epitaxial nanostructures[66–70] to also include the effects of vibrations from the surrounding material.

The polar-optical Fröhlich coupling element to longitudinal-optical (LO) phonons is given by[65]

$$g^{\mathrm{LO}}_{\boldsymbol{q}} = -i\sqrt{\frac{e^2\hbar\omega_{\mathrm{LO},\boldsymbol{q}}}{2\varepsilon_0 V}}\frac{1}{q}\sqrt{\frac{1}{\varepsilon_\infty} - \frac{1}{\varepsilon_{\mathrm{stat}}}}, \tag{16}$$

where ε_∞ is the high-frequency and $\varepsilon_{\mathrm{stat}}$ is the static dielectric constant of CdSe. The LO phonon dispersion is approximated by interpolating the known LO phonon frequencies at the high-symmetry points X and Γ by a cosine function (since Fermi's Golden Rule requires an energy continuum):

$$\omega_{\mathrm{LO},\boldsymbol{q}} = \frac{\omega^\Gamma_{\mathrm{LO}} + \omega^X_{\mathrm{LO}}}{2} + \frac{\omega^\Gamma_{\mathrm{LO}} - \omega^X_{\mathrm{LO}}}{2}\cos\left(\pi\frac{q}{q^X}\right). \tag{17}$$

The usage of bulk LO-phonon modes is substantiated, as already mentioned in the main text by results of Sigle *et al.*,[63] showing only very minor deviations in the phonon dispersion of confined modes from bulk so that ligands and polymer matrix around the platelets do not introduce severe alterations. Furthermore Fröhlich coupling already showed reasonable agreement for nanoplatelets in ref. 47, while deviations are probably caused by the way simpler Ansatz for the exciton wavefunction as compared to the Ansatz used here and scatter of data points in ref. 47.

For the exciton–photon coupling the optical matrix element in exciton basis reads:

$$M^{\alpha}_{\mathrm{l},\boldsymbol{q}} = M^{\mathrm{vc}}_{\mathrm{l},\boldsymbol{q}} \int d^2r\, \psi_\alpha(\boldsymbol{r},\boldsymbol{r}). \tag{18}$$

Two polarization modes l = TE, TM of the electric field are distinguished: the transverse electric (TE) and transverse magnetic (TM) mode. The corresponding optical matrix elements are given by[32]

$$M^{\lambda\lambda'}_{\mathrm{TE},\boldsymbol{q}} + M^{\lambda\lambda'}_{\mathrm{TM},\boldsymbol{q}} = i\sqrt{\frac{\hbar\omega_q}{2\varepsilon_0\varepsilon_\mathrm{r} V}}\left(1 + \frac{q_z}{q}\right)d_{\lambda\lambda'}, \tag{19}$$

where $d_{\lambda\lambda'}$ denotes the microscopic interband dipole moment.

Table 1 lists the CdSe material parameters used for the calculations. Since the radiative loss is emitted into the surrounding medium, the dielectric constant of the oleic acid ligands has been used for the calculation of the optical matrix element:[71] $\varepsilon_\mathrm{r} = 2.129$.

Author contributions

The manuscript was written by J.F.S., A.W.A. and M.R. A.W.A. initiated the project. R.S., A.W.A. designed the experiments and recorded the experimental spectra. M.R., M.C.C. and J.F.S. developed and performed the theoretical modeling. U.W., N. O., L.D.A.S., I.M., A.W.A. contributed to the discussion. S.C., G.H.V.B., A.V.P., A.A., I.M., M.A. provided samples and their characterization.

Conflicts of interest

There are no conflicts to declare.

Acknowledgements

We acknowledge support from the Deutsche Forschungsgemeinschaft through SFB 951 B12 (Project No. 182087777), AC290-1/1 (Project No. 265219982), AC290-2/1 (Project No. 324765876) and WO477-32/1 (Project No. 235473865), and well as Belarusian Science Foundation through the CHEMREAGENTS program and BRFFI grant No. X17KIG-004. This project has also received funding from the European Research Council (I.M., grant agreement no. 714876 PHOCONA).

Notes and references

1 S. Ithurria and B. Dubertret, *J. Am. Chem. Soc.*, 2008, **130**, 16504–16505.

2 S. Ithurria, M. D. Tessier, B. Mahler, R. P. S. M. Lobo, B. Dubertret and A. L. Efros, *Nat. Mater.*, 2011, **10**, 936.

3 A. W. Achtstein, A. Schliwa, A. Prudnikau, M. Hardzei, M. V. Artemyev, C. Thomsen and U. Woggon, *Nano Lett.*, 2012, **12**, 3151–3157.

4 M. Pelton, S. Ithurria, R. D. Schaller, D. S. Dolzhnikov and D. V. Talapin, *Nano Lett.*, 2012, **12**, 6158–6163.

5 L. T. Kunneman, M. D. Tessier, H. Heuclin, B. Dubertret, Y. V. Aulin, F. C. Grozema, J. M. Schins and L. D. A. Siebbeles, *J. Phys. Chem. Lett.*, 2013, **4**, 3574–3578.

6 A. W. Achtstein, A. V. Prudnikau, M. V. Ermolenko, L. I. Gurinovich, S. V. Gaponenko, U. Woggon, A. V. Baranov, M. Y. Leonov, I. D. Rukhlenko, A. V. Fedorov and M. V. Artemyev, *ACS Nano*, 2014, **8**, 7678–7686.

7 C. She, I. Fedin, D. S. Dolzhnikov, A. Demortière, R. D. Schaller, M. Pelton and D. V. Talapin, *Nano Lett.*, 2014, **14**, 2772–2777.

8 R. Scott, A. W. Achtstein, A. Prudnikau, A. Antanovich, S. Christodoulou, I. Moreels, M. Artemyev and U. Woggon, *Nano Lett.*, 2015, **15**, 4985–4992.

9 A. W. Achtstein, A. Antanovich, A. Prudnikau, R. Scott, U. Woggon and M. Artemyev, *J. Phys. Chem. C*, 2015, **119**, 20156–20161.

10 R. Scott, J. Heckmann, A. V. Prudnikau, A. Antanovich, A. Mikhailov, N. Owschimikow, M. Artemyev, J. I. Climente, U. Woggon, N. B. Grosse and A. W. Achtstein, *Nat. Nanotechnol.*, 2017, **12**, 1155–1160.

11 L. Biadala, F. Liu, M. D. Tessier, D. R. Yakovlev, B. Dubertret and M. Bayer, *Nano Lett.*, 2014, **14**, 1134–1139.

12 J. Q. Grim, S. Christodoulou, F. Di Stasio, R. Krahne, R. Cingolani, L. Manna and I. Moreels, *Nat. Nanotechnol.*, 2014, **9**, 891–895.

13 S. Dong, J. Lian, M. H. Jhon, Y. Chan and Z.-H. Loh, *Nano Lett.*, 2017, **17**, 3312–3319.

14 X. Ma, B. T. Diroll, W. Cho, I. Fedin, R. D. Schaller, D. V. Talapin, S. K. Gray, G. P. Wiederrecht and D. J. Gosztola, *ACS Nano*, 2017, **11**, 9119–9127.

15 S. Christodoulou, J. I. Climente, J. Planelles, R. Brescia, M. Prato, B. Martín-García, A. H. Khan and I. Moreels, *Nano Lett.*, 2018, **18**, 6248–6254.

16 J. Planelles, A. W. Achtstein, R. Scott, N. Owschimikow, U. Woggon and J. I. Climente, *ACS Photonics*, 2018, **5**, 3680–3688.

17 A. Polovitsyn, Z. Dang, J. L. Movilla, B. Martín-García, A. H. Khan, G. H. V. Bertrand, R. Brescia and I. Moreels, *Chem. Mater.*, 2017, **29**, 5671–5680.

18 A. Antanovich, A. W. Achtstein, A. Matsukovich, A. Prudnikau, P. Bhaskar, V. Gurin, M. Molinari and M. Artemyev, *Nanoscale*, 2017, **9**, 18042.

19 A. W. Achtstein, O. Marquardt, R. Scott, M. Ibrahim, T. Riedl, A. V. Prudnikau, A. Antanovich, N. Owschimikow, J. K. N. Lindner, M. Artemyev and U. Woggon, *ACS Nano*, 2018, **12**, 9476–9483.

20 R. Scott, S. Kickhofel, O. Schoeps, A. Antanovich, A. Prudnikau, A. Chuvilin, U. Woggon, M. Artemyev and A. W. Achtstein, *Phys. Chem. Chem. Phys.*, 2016, **18**, 3197–3203.

21 M. D. Tessier, B. Mahler, B. Nadal, H. Heuclin, S. Pedetti and B. Dubertret, *Nano Lett.*, 2013, **13**, 3321–3328.

22 A. Prudnikau, A. Chuvilin and M. Artemyev, *J. Am. Chem. Soc.*, 2013, **135**, 14476–14479.

23 F. Rajadell, J. I. Climente and J. Planelles, *Phys. Rev. B*, 2017, **96**, 035307.

24 M. G. Bawendi, M. L. Steigerwald and L. E. Brus, *Annu. Rev. Phys. Chem.*, 1990, **41**, 477–496.

25 A. L. Efros, M. Rosen, M. Kuno, M. Nirmal, D. J. Norris and M. Bawendi, *Phys. Rev. B: Condens. Matter Mater. Phys.*, 1996, **54**, 4843–4856.

26 A. Sitt, A. Salant, G. Menagen and U. Banin, *Nano Lett.*, 2011, **11**, 2054–2060.

27 H. Eshet, M. Grünwald and E. Rabani, *Nano Lett.*, 2013, **13**, 5880–5885.

28 S. Nakamura, M. Senoh, N. Iwasa and S. ichi Nagahama, *Jpn. J. Appl. Phys.*, 1995, **34**, L797.

29 S. T. Tan, X. W. Sun, H. V. Demir and S. P. DenBaars, *IEEE Photonics J.*, 2012, **4**, 613–619.

30 S. Nakamura, *Rev. Mod. Phys.*, 2015, **87**, 1139–1151.

31 H. Haug and S. W. Koch, *Quantum Theory of the Optical and Electronic Properties of Semiconductors*, World Scientific, Singapore, 1994.

32 R. Zimmermann, E. Runge and V. Savona, *Quantum Coherence Correlation and Decoherence in Semiconductor Nanostructures*, 2003, pp. 89–165.

33 R. Zimmermann, F. Grosse and E. Runge, *Pure Appl. Chem.*, 1997, **69**, 1179–1186.

34 S. Priyadarshi, A. M. Racu, K. Pierz, U. Siegner, M. Bieler, H. T. Duc, J. Förstner and T. Meier, *Phys. Rev. Lett.*, 2010, **104**, 217401.

35 R. Singh, M. Richter, G. Moody, M. E. Siemens, H. Li and S. T. Cundiff, *Phys. Rev. B*, 2017, **95**, 235307.

36 M. Richter, R. Singh, M. Siemens and S. T. Cundiff, *Sci. Adv.*, 2018, **4**, eaar7697.

37 G. H. V. Bertrand, A. Polovitsyn, S. Christodoulou, A. H. Khan and I. Moreels, *Chem. Commun.*, 2016, **52**, 11975–11978.

38 M. Richter, *Phys. Rev. Mater.*, 2017, **1**, 016001.

39 A. W. Achtstein, R. Scott, S. Kickhöfel, S. T. Jagsch, S. Christodoulou, G. H. V. Bertrand, A. V. Prudnikau, A. Antanovich, M. Artemyev, I. Moreels, A. Schliwa and U. Woggon, *Phys. Rev. Lett.*, 2016, **116**, 116802.

40 A. Naeem, F. Masia, S. Christodoulou, I. Moreels, P. Borri and W. Langbein, *Phys. Rev. B: Condens. Matter Mater. Phys.*, 2015, **91**, 121302.

41 B. T. Diroll, W. Cho, I. Coropceanu, S. M. Harvey, A. Brumberg, N. Holtgrewe, S. A. Crooker, M. R. Wasielewski, V. B. Prakapenka, D. V. Talapin and R. D. Schaller, *Nano Lett.*, 2018, **18**, 6948–6953.

42 R. Zimmermann and E. Runge, *Phys. Status Solidi A*, 1997, **164**, 511–516.

43 H. Haug and S. W. Koch, *Quantum Theory of the Optical and Electronic Properties of Semiconductors*, World Scientific, Singapore, 2004.

44 O. Mayrock, H.-J. Wünsche, F. Henneberger, C. Riva, V. A. Schweigert and F. M. Peeters, *Phys. Rev. B: Condens. Matter Mater. Phys.*, 1999, **60**, 5582–5589.

45 E. V. Shornikova, L. Biadala, D. R. Yakovlev, V. F. Sapega, Y. G. Kusrayev, A. A. Mitioglu, M. V. Ballottin, P. C. M. Christianen, V. V. Belykh, M. V. Kochiev, N. N. Sibeldin, A. A. Golovatenko, A. V. Rodina, N. A. Gippius, A. Kuntzmann, Y. Jiang, M. Nasilowski, B. Dubertret and M. Bayer, *Nanoscale*, 2018, **10**, 646–656.

46 T. Takagahara, *Phys. Rev. B: Condens. Matter Mater. Phys.*, 1993, **47**, 4569–4584.

47 R. Scott, A. V. Prudnikau, A. Antanovich, S. Christodoulou, T. Riedl, G. H. V. Bertrand, N. Owschimikow, J. K. N. Lindner, Z. Hens, I. Moreels, M. Artemyev, U. Woggon and A. W. Achtstein, *Nanoscale*, 2019, **11**, 3958–3967.

48 H. Carmichael, *Statistical Methods in Quantum Optics 1 - Master Equation and Fokker-Planck Equations*, Springer, Berlin Heidelberg New York, 1999.

49 H.-P. Breuer and F. Petruccione, *The Theory of Open Quantum Systems*, Oxford University Press, Oxford, 2002.

50 S. Balay, S. Abhyankar, M. F. Adams, J. Brown, P. Brune, K. Buschelman, L. Dalcin, V. Eijkhout, W. D. Gropp, D. Kaushik, M. G. Knepley, L. C. McInnes, K. Rupp, B. F. Smith, S. Zampini and H. Zhang, PETSc Web page, 2015, http://www.mcs.anl.gov/petsc, http://www.mcs.anl.gov/petsc.

51 S. Balay, S. Abhyankar, M. F. Adams, J. Brown, P. Brune, K. Buschelman, L. Dalcin, V. Eijkhout, W. D. Gropp, D. Kaushik, M. G. Knepley, L. C. McInnes, K. Rupp, B. F. Smith, S. Zampini and H. Zhang, *PETSc Users Manual, Argonne National Laboratory Technical Report ANL-95/11 - Revision 3.6*, 2015.

52 M. D. Tessier, C. Javaux, I. Maksimovic, V. Loriette and B. Dubertret, *ACS Nano*, 2012, **6**, 6751–6758.

53 F. T. Rabouw, J. C. van der Bok, P. Spinicelli, B. Mahler, M. Nasilowski, S. Pedetti, B. Dubertret and D. Vanmaekelbergh, *Nano Lett.*, 2016, **16**, 2047–2053.

54 U. Bockelmann and T. Egeler, *Phys. Rev. B: Condens. Matter Mater. Phys.*, 1992, **46**, 15574–15577.

55 P. Guyot-Sionnest, M. Shim, C. Matranga and M. Hines, *Phys. Rev. B: Condens. Matter Mater. Phys.*, 1999, **60**, R2181–R2184.

56 D. J. Norris and M. G. Bawendi, *Phys. Rev. B: Condens. Matter Mater. Phys.*, 1996, **53**, 16338–16346.

57 G. Rainò, I. Moreels, A. Hassinen, T. Stöferle, Z. Hens and R. F. Mahrt, *Nano Lett.*, 2012, **12**, 5224–5229.

58 M. D. Tessier, L. Biadala, C. Bouet, S. Ithurria, B. Abecassis and B. Dubertret, *ACS Nano*, 2013, **7**, 3332–3340.

59 A. Steinhoff, M. Florian, A. Singh, K. Tran, M. Kolarczik, S. Helmrich, A. W. Achtstein, U. Woggon, N. Owschimikow, F. Jahnke and X. Li, *Nat. Phys.*, 2018, **14**, 1199.

60 E. V. Shornikova, L. Biadala, D. R. Yakovlev, D. Feng, V. F. Sapega, N. Flipo, A. A. Golovatenko, M. A. Semina, A. V. Rodina, A. A. Mitioglu, M. V. Ballottin, P. C. M. Christianen, Y. G. Kusrayev, M. Nasilowski, B. Dubertret and M. Bayer, *Nano Lett.*, 2018, **18**, 373–380.

61 J. Feldmann, G. Peter, E. O. Göbel, P. Dawson, K. Moore, C. Foxon and R. J. Elliott, *Phys. Rev. Lett.*, 1987, **59**, 2337–2340.

62 S. A. Cherevkov, M. V. Artemyev, A. V. Prudnikau and A. V. Baranov, *Phys. Rev. B: Condens. Matter Mater. Phys.*, 2013, **88**, 041303.

63 D. O. Sigle, J. T. Hugall, S. Ithurria, B. Dubertret and J. J. Baumberg, *Phys. Rev. Lett.*, 2014, **113**, 087402.

64 T. Takagahara, *Phys. Rev. B: Condens. Matter Mater. Phys.*, 1985, **31**, 6552–6573.

65 G. D. Mahan, *Many-Particle Physics*, Kluwer Academic/ Plenum Publishers, New York, 2000.

66 B. Krummheuer, V. M. Axt and T. Kuhn, *Phys. Rev. B: Condens. Matter Mater. Phys.*, 2002, **65**, 195313.

67 J. Förstner, C. Weber, J. Danckwerts and A. Knorr, *Phys. Rev. Lett.*, 2003, **91**, 127401.

68 I. Waldmüller, J. Förstner, S.-C. Lee, A. Knorr, M. Woerner, K. Reimann, R. Kaindl, T. Elsaesser, R. Hey and K. Ploog, *Phys. Rev. B: Condens. Matter Mater. Phys.*, 2004, **69**, 205307.

69 P. Gartner, J. Seebeck and F. Jahnke, *Phys. Rev. B: Condens. Matter Mater. Phys.*, 2006, **73**, 115307.

70 R. Rosati, D. E. Reiter and T. Kuhn, *Phys. Rev. B*, 2017, **95**, 165302.

71 *The Merck Index - An Encyclopedia of Chemicals*, 2006, https://www.rsc.org/Merck-Index.

72 D. Katz, T. Wizansky, O. Millo, E. Rothenberg, T. Mokari and U. Banin, *Phys. Rev. Lett.*, 2002, **89**, 086801.

73 R. Benchamekh, N. A. Gippius, J. Even, M. O. Nestoklon, J.-M. Jancu, S. Ithurria, B. Dubertret, A. L. Efros and P. Voisin, *Phys. Rev. B: Condens. Matter Mater. Phys.*, 2014, **89**, 035307.

74 C. F. Cline, H. L. Dunegan and G. W. Henderson, *J. Appl. Phys.*, 1967, **38**, 1944–1948.

75 J. Li and L.-W. Wang, *Appl. Phys. Lett.*, 2004, **85**, 2929–2931.

76 *Cadmium selenide (CdSe) optical properties, general, refractive index: Datasheet from Landolt-Börnstein - Group III Condensed Matter·Volume 41B: II-VI and I-VII Compounds; Semimagnetic Compounds*, 1999, https://materials.springer.com/lb/docs/sm_lbs_978-3-540-31359-5_610.